



Localization and quantification of radical production in cavitating flows with luminol chemiluminescent reactions

Darjan Podbevšek^{a,1,*}, Damien Colombet^b, Frederic Ayela^b, Gilles Ledoux^a

^a Institut Lumière Matière, Université Claude Bernard Lyon 1, 69622 Villeurbanne, France

^b Laboratoire des Écoulements Géophysiques et Industriels, Univ. Grenoble Alpes, CNRS, 38000 Grenoble, France

ARTICLE INFO

Keywords:

Microfluidics

Hydrodynamic cavitation

Luminol chemiluminescence

Photon yield

Radical production

Advance oxidizing processes

ABSTRACT

Hydrodynamic cavitation experiments in microfluidic systems have been performed with an aqueous solution of luminol as the working fluid. In order to identify where and how much reactive radical species are formed by the violent bubble collapse, the resulting chemiluminescent oxidation reaction of luminol was scrutinized downstream of a constriction in the microchannel. An original method was developed in order to map the intensity of chemiluminescence emitted from the micro-flow, allowing us to localize the region where radicals are produced. Time averaged void fraction measurements performed by laser induced fluorescence experiments were also used to determine the cavitation cloud position. The combination void fraction and chemiluminescence two-dimensional mapping demonstrated that the maximum chemiluminescent intensity area was found just downstream of the cavitation clouds. Furthermore, the radical yield can be obtained with our single photon counting technique. The maximum radical production rates of $1.2 \cdot 10^7$ OH[•]/s and radical production per processed liquid volume of $2.15 \cdot 10^{10}$ HO[•]/l were observed. The proposed technique allows for two-dimensional characterisation of radical production in the microfluidic flow and could be a quick, non-intrusive way to optimise hydrodynamic cavitation reactor design and operating parameters, leading to enhancements in wastewater treatments and other process intensifications.

1. Introduction

The appearance of the vapor phase due to a pressure decrease in the liquid is referred to as cavitation. In practise, vapor bubbles can be induced by acoustic excitation (20 kHz–1 MHz) in a process called ultrasonic or acoustic cavitation (AC), where the rarefactions in the soundwaves act as low-pressure regions. Alternatively, hydrodynamic cavitation (HC) can occur due to Bernoulli's principle, where the pressure decrease originates from the fluid acceleration through a constriction. For both cases, the dynamics of vapor bubbles, primarily the violent bubble collapse upon pressure recovery, is associated with unwanted as well as beneficial physical phenomena. As the interface shrinks in the rapidly imploding bubble, a compression of the uncondensed content allows these bubbles to be used as high temperature/pressure reactors, producing exotic and/or active species, such as radicals [1]. These chemical effects are well established with acoustically driven cavitation, opening a separate field in chemistry called sonochemistry. In aqueous solutions, the periodic bubble motion is known to

produce radical species (primarily, but not limited to, hydroxyl radicals) by homolytic splitting of water vapor [2]. The produced radicals can recombine to form secondary reactive species [3], fuelling various chemical reactions, which are thought to be crucial for waste-water treatment and advance oxidising processes [4,5]. Concerning HC, due to the multitude of parameters governing the process of cavitation, it is known to be a notoriously complex topic to study [6], often leading to unreproducible or even conflicting results between studies. These parameters are physical and chemical properties of the fluid (vapor pressure, tensile strength of the pure liquid, surface tension, viscosity, density, dissolved gas content, chemical impurities) [7,8]. Nucleation parameters such as uncondensed gas pockets and/or solid nuclei type are also involved [9]. Furthermore, some parameters from AC, such as frequency, cannot be directly applicable to HC. Some authors suggest that residence time of the fluid in the low pressure region as a means of comparison [10]. Due to the rapid oscillations in the acoustic field it is generally accepted that AC produces smaller, yet rapid and periodic bubble oscillations, while HC is expected to produce larger bubbles at

* Corresponding author.

E-mail address: darjan.podbevsek@fs.uni-lj.si (D. Podbevšek).

¹ Present address: Faculty of Mechanical Engineering, University of Ljubljana, 1000 Ljubljana, Slovenia.

<https://doi.org/10.1016/j.ultsonch.2020.105370>

Received 5 June 2020; Received in revised form 9 September 2020; Accepted 11 October 2020

Available online 21 October 2020

1350-4177/© 2020 The Authors.

Published by Elsevier B.V. This is an open access article under the CC BY-NC-ND license

(<http://creativecommons.org/licenses/by-nc-nd/4.0/>).

longer timescales. Moreover, it has been suggested that HC could be even more energy efficient than AC, especially for scale up to industrial processes, where large volumes of liquids have to be processed [10,11]. On the same note, a limited number of publication on the topic of HC induced chemistry has been outlined more than two decades ago, by Suslick et al. [12]. Since then, several publications on the effect of reactor geometry and multiple orifice design have been studied [11,13–15]. Hydroxyl formation has been indirectly observed in low pressure HC devices, with constriction velocities below 30 m/s [16,17]. Nano-emulsions and dispersed product generation has also been studied and seems to be aided by HC [18–22]. A typical HC experiment consists of a loop with the HC reactor and a reservoir refilled with a centrifugal pump. In such installations it is possible to have additional cavitation occurring in the pump; to our knowledge only one group has taken into account this effect [23,24]. Numerous different approaches have been used to probe the chemical activity in HC, usually by measuring the radical yield of the process. The analysis of chemical products often involves the increase or the degradation of certain chemical species known to be affected by the presence of radicals [25,26]. Triiodide formation otherwise known as the Weissler reaction has been a popular method [13], but has come into question for measuring the efficiency of HC, as the tri iodide complex was shown to be consumed even without the presence of cavitation [27]. The degradation of p-nitrophenol [28], Rhodamine B [26], BTEX (benzene, toluene, ethylbenzene, xylene) [23], were all studied, as well as the transformation of benzene into phenol [16] and terephthalic acid dosimetry [7]. The latter as well as the salicylic acid dosimetry [10,25] use specific scavengers of OH[•] to estimate the hydroxyl radical production by spectroscopic analysis of the products. However, most techniques require fluid extraction to quantify the radical production rate, which can be intrusive and time consuming. For this reason luminol has often been used, as it is well known for its chemiluminescent (CL) reaction when oxidised. In AC it is used to show radical rich regions in reactors, i.e. the bubble collapse regions [3,8,29–32]. However, it is only recently that the generation of hydroxyl radicals in high pressure homogenizers has been investigated [19]. The benefit of luminol CL is that the emitted photon can be used to quantify the number of oxidation reaction and therefore the number of radicals reacting. This approach was used in [33], at different channel geometries and driving pressures, allowing the quantification of the global radical production in the microfluidic devices. Generally, experiments considering cavitation at the microscale are limited, although they present some advantages over experiments performed with macroscale flows, especially for fundamental research. Foremost, HC ‘on a chip’ allows easier control over some parameters in the experimental setup, as well as making possible the use of low quantities of specialised liquids [34,35]. To prevent clogging, the geometries of the microchannels often require filtration of the working liquid. Combined with the smoother channel walls produced by the etching process, the system contains fewer and also smaller nuclei, leading to higher tensile strength of the liquid and to a metastable system [36]. Also, faster bubble dynamics with shorter lifetimes are expected, compared to macroscopic systems. Finally, the microfluidic channels can often ease the implementation of optical probing methods. In spite of these advantages, the research field on the topic of cavitation in microchannels involves only a few groups [33–61].

In this article, we build on the global radical quantization method developed by Podbevšek et al. [33], towards the mapping of the CL activity. By using a simple optical setup and a point by point scanning technique, we have been able to obtain 2D maps of CL activity in the channel. With a luminescence intensity based void fraction mapping technique, we show the radical production in the microchannels correlates to the vapor bubble collapse. In this way it is possible to localise the radical production areas in the micro-cavitating flow.

2. Material and methods

Microfluidic setup: The channel design used was a micro-diaphragm (MD) type constriction, which promotes the formation of cavitation and has been studied in previous publications [33,35,36,38,50]. Typically, channel design follows a common shape; a milli channel of uniform height H and width W of about 0.5 mm containing a thin wall (20–100 μm) micro constriction in the middle. The geometrical dimensions of the two microchannels under investigation are listed in Table 1. The long (MD-A) and short (MD-B) diaphragm design differ mainly in the run off length of the milli channels upstream and downstream of the diaphragm and its dimensions, but not in constriction design or production method. The fabrication of the microfluidic channels is based on MEMS techniques and described in detail in previous publications [36,48]. For a non-transparent Pyrex-Si channel, using a lithography process, the desired channel design is transferred onto a 400 μm thick silicon wafer with S1818 photoresist and a UV irradiation of $\sim 30 \text{ mJ/cm}^2$. Then the silicon substrate is etched by the so-called Bosch process (deep reactive ion etching), which allows highly anisotropic microstructures with low scalloping rates, forming nearly vertical side walls. The final step is the anodic bonding of a Pyrex glass sheet to the top side of the channel, with pre-drilled inlet and outlet holes. A sufficient diameter is chosen for the inlet/outlet holes to avoid cavitation in this part of the channel. Metallic tubes with a Viton O-ring are clamped on top of the inlet/outlet holes by the channel holder assembly in order to connect it to the fluid recirculation system. A nitrogen gas bottle and a pressure regulating valve was used to set the driving pressure in the system. An 8L pressure tank with a flexible butyl rubber membrane containing the working liquid allows for the pressure to be exerted on the liquid while preventing liquid/gas contact. Before entering the microchannel the liquid is filtered with a combination of a glass microfibre 2,7 μm and a 10 μm nylon mesh filters. This prevents clogging of the MD while also removing particles that can act as cavitation nuclei; consequently, the liquid in our system exhibits metastable behaviour [36] and a flow hysteresis. The relationship between the total pressure drop $\Delta P = P_{in} - P_{out}$ and the flowrate Q is mainly monitored by the micro diaphragm constriction (investigated in the preceding study [36]), and obeys:

$$\Delta P = \frac{\rho}{2C_d^2} \frac{Q^2}{(wH)^2} \quad (1)$$

where ρ is the fluid density, w the width of the diaphragm at the constriction, H the height of the channel. The discharge coefficient (C_d) remains constant at high Reynolds numbers, as long as the length of the constriction is short compared to its diameter [33]. The experimental ΔP (Q) relationship has been measured for each microchannel in order to compare it to theory. As expected, a stabilisation of C_d near 0.75–0.78 is observed for Reynolds numbers above 1000. The Reynolds number is defined as:

$$Re = \frac{\rho u_0 D_h}{\mu} \quad (2)$$

where μ is the dynamic viscosity of the fluid u_0 is the average velocity of

Table 1

Microchannel geometry dimensions in μm : w_c – constriction width, l_c – constriction length, W – inlet/outlet channel width, L_i/L_o – inlet/outlet channel length, H – channel height, D_h – hydraulic diameter. The flow parameters C_d – discharge coefficient, ΔP_{cav} , Q_{cav} and σ_{cav} – the calculated pressure, flow and cavitation number at cavitation inception [36].

Channel	w_c	l_c	W	L (L_i/L_o)	H
MD-A	101	58	500	15000/25000	164
MD-B	54	94	500	1500/1500	150
-	D_h	C_d [-]	ΔP_{cav} [bar]	Q_{cav} [$\mu\text{l/s}$]	σ_{cav} [-]
MD-A	125	0.753	3.2	317.2	0.536
MD-B	79	0.782	5.8	216.2	0.276

the fluid and D_h the hydraulic diameter at the constriction. Above the cavitation threshold pressure, a shear type cavitation appears in the channel. While increasing the flow rate, a cavitation pocket starts forming on one side of the emerging jet downstream the constriction, curving the jet towards one of the channel side walls. As the flow rates increases, a second but less intense vapor cloud formation appears on the other side of the jet. At very high flow rates (that case was not treated in this study), the two vapor pockets become symmetric along the central liquid jet [50]. To characterise cavitation intensity in our microchannels, we can use the cavitation number σ :

$$\sigma = \frac{2(P_{out} - P_{vap})}{\rho u^2} \approx \frac{2P_{out}}{\rho u^2} \approx \frac{P_{out}}{C_d^2 \Delta P} \quad (3)$$

A detailed analysis on the cavitation number can be found in dedicated publications on hydrodynamic cavitation [36,37]. The cavitation number σ corresponds to the ratio between the static pressure decrease required to enable cavitation and the pressure decrease generated by the flow. Equation (3) can be simplified because in our experiment, the vapor pressure is significantly lower than P_{out} . The subscript cav indicates the critical value of a parameter above or below which cavitation occurs (P_{cav} , Q_{cav} , σ_{cav}). As the absolute value of σ is only related to $1/\Delta P$, it will be more convenient to calculate the ratio σ_{cav}/σ , when comparing the behaviour of different channels. For a microdiaphragm, it has been calculated that $\sigma_{cav} = 2w/C_d W$ [36].

Liquid preparation: Ultrapure 18.2M Ω (0.2 μ m) water was used as the working liquid, prepared by a Barnstead Smart2Pure water purification system from Thermo Scientific. A 1 mM aqueous solution of luminol was prepared by dissolving 177 mg of luminol powder (3-aminophthalhydrazide 97% from Sigma-Aldrich) in 15 ml of 3.75 mM NaOH solution and then diluted to make 1L of solution with a pH of around 11.7. The pH can shift toward acidic values during operations, so it was monitored in order to remain above 11. The hydrodynamic properties (such as viscosity) of the solution was shown not to differ significantly from ultrapure water properties, as was also indicated by the fact that the metastable behaviour is still present. Compared to the expected radical yields, using such concentrations puts the reactive luminol molecules in excess, providing ample supply for the reactions with the short-lived radicals. Dissolved gas concentration in the liquid was not controlled during the experiment. Liquid temperature was stable at 20 °C throughout the experiment.

Optical setup: The light emission from the CL reaction, produced as luminol undergoes an oxidative reaction by the free radicals, was acquired by a simple optical setup, involving a photomultiplier tube (PMT) and a long working distance (LWD) objective (Fig. 1). A 20 \times NA 0.6 LWD objective from OPTEM was used to capture 9.99% of the light emitted from the channel. Compared to the global acquisition technique used in previous study [33], where the PMT was simply placed, without optics as close as possible to the diaphragm opening, the current technique has a higher solid collection angle, but has losses in transmission, corresponding to roughly 50% for the luminol emission range (425 nm peak). Also, this technique allows for simple mapping to be performed, by moving the microchannels and recording the photon yield in each point of interest. Prior to the mapping, channel coordinates have to be acquired. For this purpose, a setup with an optical fibre was used, which has at one end a 473 nm laser injected into the fibre and on the other optics recollimating the beam and directing it through a beam splitter to the objective (right side in Fig. 1 – Alignment). The beam was then focused and reflected from the polished silicon surface of the studied microchannel, back to the objective and on to a MotiCam 1SP CMOS camera, which allows us to record the position of the channel walls. During the experiment, the laser injection module and the beam splitter are removed and replaced by a PMT R9789 from EMI with a 1250 V driving voltage (Fig. 1 - Acquisition). The quantum efficiency of the PMT is \sim 15% for the emission range of luminol chemiluminescence (peak at 425 nm) [33]. Pulses created by the detector are amplified by an ORTEC

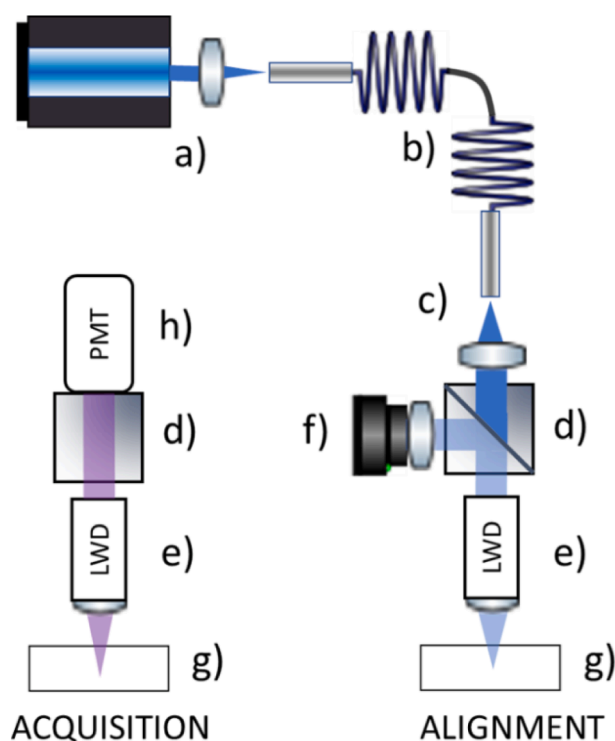


Fig. 1. Optical part of the experimental setup. On the right the setup for coordinate plotting in the channel and on the left the simple acquisition setup with a photomultiplier tube (PMT). The individual elements marked in the figure: a) 473 nm laser light source, b) optical fiber, c) collimation optics, d) beamsplitter mount, e) long working distance (LWD) objective, f) CMOS camera, g) microchannel sample with x, y, z motion control, h) photomultiplier.

VT120C fast preamplifier and the resulting signal is directed to an ORTEC 935Quad CFD discriminator. A counter on the NI USB-6343 DAQ was used to acquire the photon flux. As the detection device is sensitive to single photons, light tight conditions had to be assured around the channel. Light emission only occurs when cavitation is present in the flow. The movement of the sample assembly in the planar direction is assured by Z825B motorized actuators from Thorlabs. The height of the channel was set by a mechanical positioning platform and was always fixed to the middle of the channel height, as it was found to yield the highest signal strength. Luminescence from pure water in cavitating flow was not observed in our experiments [33].

Radical yield: The principle behind the radical yield quantization is based on the fact that a single emitted photon from the channel will be a consequence of a single non-specific free radical oxidising the luminol molecule. We can convert the recorded yield to the radical production of the channel, with appropriate correction factors. The first of these is the correction for the optical acquisition system. As the photon yield in the microchannels is very low, a compromise had to be made. The spatial filters defining the acquisition voxel of an optical system, had to be removed in order to substantially increase the incoming light. This allowed us to detect the weak signal emitted from the micro-cavitating flow, while sacrificing the resolving power of the optical system, leading to anomalies, like observing some signal outside the bounds of the microfluidic channel. The resolution of the optical system can be described by a 2D Gaussian of $\Sigma=261 \mu$ m. The probability to detect a photon emitted from a position (0,0) with the detector positioned at a position (x,y) is then given by $I = \frac{1}{(2\pi\Sigma^2)} e^{-1/2(\frac{x^2+y^2}{\Sigma^2})}$. The number of photons emitted per second by the whole channel is given then by the total number of photons detected over the map multiplied by the prefactor $1/(2\pi\Sigma^2)$ and divided by the acquisition density (number of points acquired per scanned area). Furthermore, the radical yield is obtained by

dividing the photon yield with other compensation factors; 0.15 for the PMT efficiency, 0.099 and 0.5 for the optical acquisition and transmission of the objective and lastly 0.0124 for the luminol chemiluminescence yield [62]. Furthermore, the radical yield per treated volume can be obtained by dividing with the volumetric flow.

Void Fraction: For similar flow conditions, shadowgraph images have been acquired using the identical installation as described in [50]. A MiroM310 Phantom camera (150 μ s exposure time) was mounted on an Olympus SZX binocular (X90) with a high power led light KOMii Cyclop1. The background removal was performed as well as an average on 10 000 uncorrelated images (1000 fps) to get a picture corresponding to the shadow of the bubble clouds present in the microchannel. Furthermore, a void fraction mapping technique was used to locate and quantify the cavitation clouds, appearing just downstream of the constriction. For these experiments a LIF (laser induced fluorescence) method was developed, based on a confocal microscope setup and performed on ultrapure water seeded with luminescent nanoprobe, described in a previous publication [35]. The void fraction measurements are

estimated from the luminescence intensity averaged over the acquisition time at a given position. As reported by [35], due to the fact that the vapor/gas phase does not contain any light emitting species, the drop of the recorded light intensity in a voxel is correlated to the void fraction averaged over the acquisition time. The fluorescence intensity measurements in the channel have been acquired point by point every 50 μ m in the X direction and 20 μ m in the Y direction (flow direction), producing a void fraction map of the region downstream of the constriction.

3. Results and discussion

One of the main shortfalls with the previously developed method [33] was the inability to locate the origin of the light emission. Therefore, there was a possibility that some of the chemiluminescent reactions were taking place much further downstream, outside the measurement area provided by the optical device. Hydroxyl radical has a reported half-life running from ns [63] to μ s [64,65], depending on the nature of the reaction involved and on the concentration of the reactants. Also,

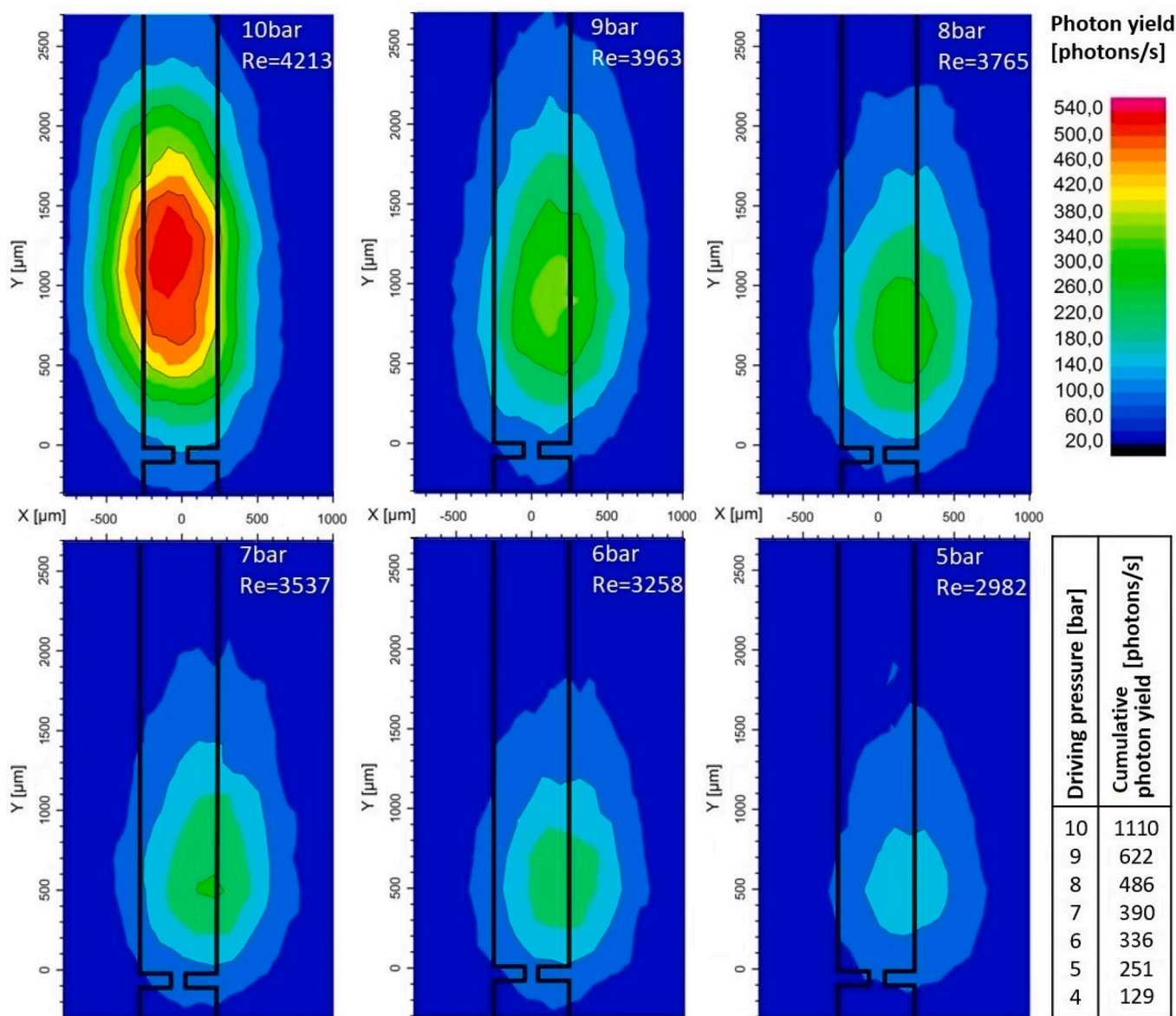


Fig. 2. The contour plot of the chemiluminescence intensity in the MD-A as a function of ΔP (4 bar plot omitted for clarity). Flow direction is from bottom to top, with the black lines represent the channel walls. The measurement points were acquired every 100 μ m in the x and 200 μ m in the y coordinate, and the photon yield averaged over 3 s. The cumulative CL yield with subtracted background signal values for each driving pressure is tabled in the lower right corner.

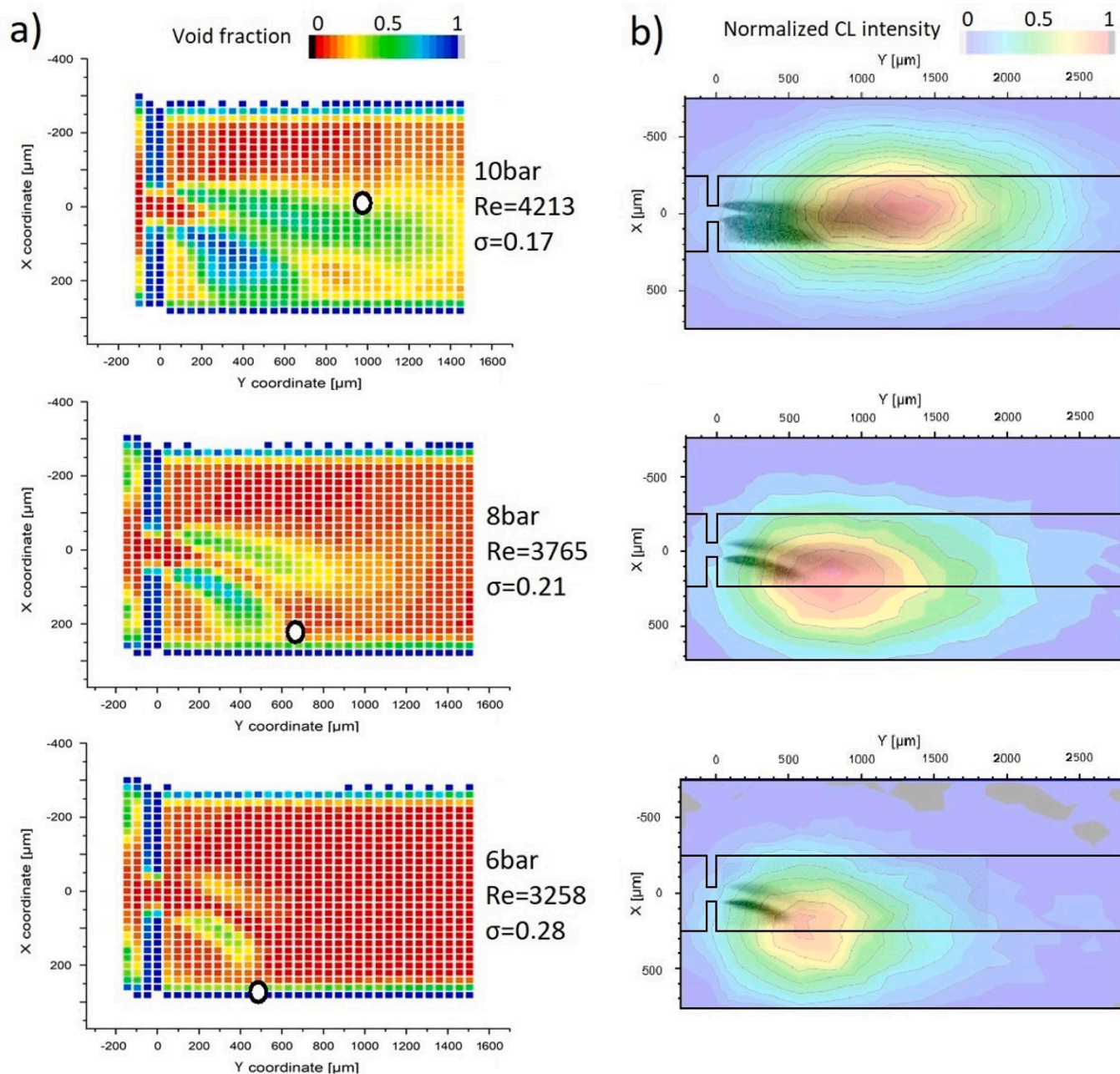


Fig. 3. a) The overlap of the void fraction mapping and the maximum CL activity position (black circle) of the 2d gaussian data fit for MD-A. b) shadowgraphy average image (black indicating high void fraction regions) of the flow in microchannels (average cloud cover) overlapped with the contour maps of the CL activity in MD-A. The bubble collapse region, indicated by the maximum CL activity, is observed at the end of the main cavitation cloud. Flow is from left to right.

when considering the channels size (Table 1) and the maximum flow at the constriction (15–35 μm/μs), the CL activity is expected to be within the confines of the microchannel. In hydrodynamic cavitation ‘on a chip’, high speed camera imaging [38] has demonstrated that, what appears to be a steady state vapour cloud, is in fact a succession of bursting vapour bubbles. However, it is difficult to localize where they collapse. For this reason, we used an optical scanning technique presented above to make point by point measurements of the CL activity in the area just downstream of the diaphragm, where the cavitation cloud is present. Results are presented in Fig. 2, where the CL activity contour maps are shown for different driving pressures applied to the device MD-A. The acquisition of each point was averaged over 3 s, with a 100 μm step between the measured points along the X-axis and 200 μm step along the Y-axis (direction of the flow). The scanned area was 1.8 mm along the X axis, against 3 mm along the Y axis. To increase the

sensitivity of the inherently weak CL signal emitted, the spatial filtering components, which are usually present in such setups, have been removed. As explained above, this makes the acquisition volume of our microscope non-confined, leading to a not well-defined spatial resolution, as is evident on the CL maps in Fig. 2, where the CL activity is recorded even when the focal point is located outside the channel bounds (black lines). The spatial distribution of the void fraction in the MD-A device is displayed in Fig. 3a, for different cavitating flow regimes. The location of the maximum CL activity, that has been recorded in Fig. 2, has been reported on each picture in the form of a black circle. The peak of the CL activity is always located at the end of the main vapour cloud, indicating that the majority of the vapor bubbles are likely to collapse in this area. Similar findings are presented in Fig. 3b, where the shadowgraphy images of the flow averaged over 10,000 frames are presented, showing the time averaged vapor cloud distribution. Here

once more, the overlap of shadowgraphy pictures and of CL maps demonstrates that the highest activity on the CL map is located just downstream of high void fraction regions. The emerging jet downstream the microdiaphragm has the tendency to curve towards a preferential side in the channel and usually remains on that side until the flow is turned off. This is due to low pressure vortices, trapped between the jet and the wall, initiating the cavitation pocket (Fig. 3 at 6 bar). By increasing the flow velocity, the recirculating area on the opposite side of the channel becomes increasingly important, until a second vapor pocket arises (Fig. 3 at 8 bar); then, the emerging flow is balanced by two gaseous pockets at the same saturation pressure, and is straightened (Fig. 3 at 10 bar). Our experimental results display an obvious correlation between the direction of the emerging flow, the size of the vapour cloud and the maximum chemiluminescent activity area. Considering the fast reaction kinetics of the hydroxyl radical it is unlikely that the observed CL activity is taking place in a recirculating vortex. It was not possible to monitor the flow at pressure above 10 bar, due to the limitations of the liquid line of our experiment, but visual observations have shown the cavitation clouds are gradually moving towards supercavitation pockets that levels out on both sides of the central liquid jet. The transition to the former flow regime seems to be less obvious with the shorter length channel MD-B, as is seen in Fig. 4. A simple 2D gaussian fit of the recorded maps was used to plot the maxima of the CL

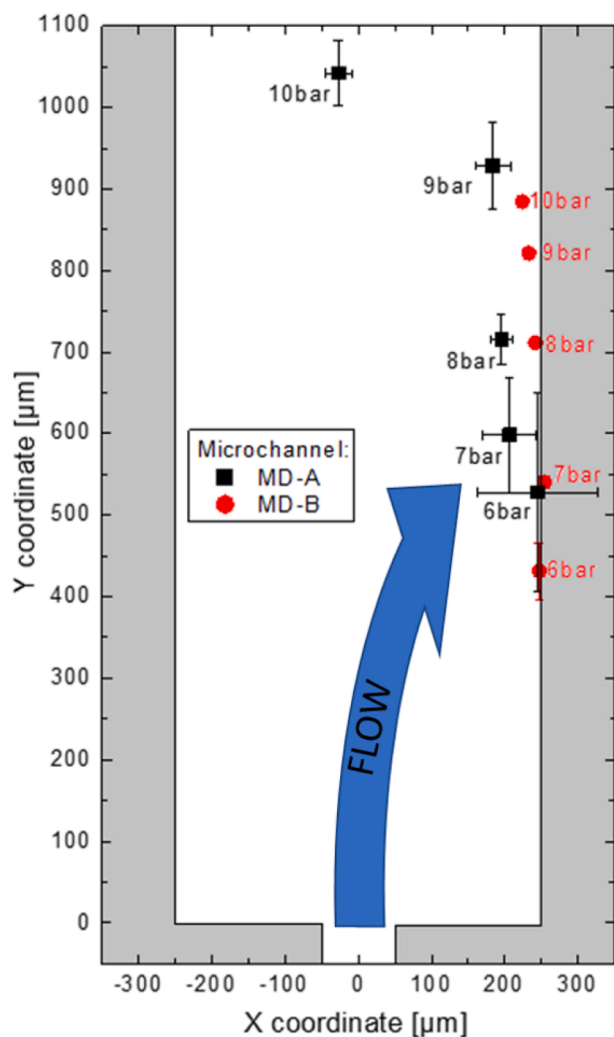


Fig. 4. The position of the maximum CL activity downstream the constriction as a function of increasing pressure MD-A and MD-B. A 2D gaussian plot of the acquired data points was performed to approximate the position of the CL emission area. Gray area presents the channel walls. Flow is the y-axis.

activity moving inward to the channel centre with increasing pressure, as before but at a lesser rate. This might be due to the channel design, which exhibits a lower σ_{cav} value to that of channel MD-A. However, the distance of this peak from the diaphragm opening increases linearly, as does the distance to the cavitation cloud end (Fig. 5), with increasing driving pressure for both channels. The linear increase of the velocity at the constriction causes a corresponding cloud expansion. For practical reasons the cavitation cloud length (measured by LIF), is defined by the measured points with the void fraction above 0.3 and the stronger, inner cloud of the two cavitating clouds was considered. From Fig. 5, the average lifetimes of the bubbles inception at the constriction can be approximated. Assuming the bubbles translation velocity is equal to the velocity of the jet at the constriction, and the travel distance over the cavitation cloud length, we get bubble lifetimes (20–27 μ s) reminiscent of a half-period (rarefaction) in a typical low frequency AC (20 kHz), as opposed to millisecond times in HC at macroscale [10]. However, even if the physics of the bubbles collapses in HC and AC is similar, the pressure variation seen by bubbles is much more complicated, since it depends on both bubble trajectories and pressure fields imposed by the flow. This can lead to much faster collapse times, as the pressure variations are not sinusoidal as in AC, leading to higher effective equivalent frequencies. The distance between the cloud end and the maximum CL activity are consistent with radical lifetimes in the μ s range, indicating that the majority of the produced radicals are highly reactive and therefore hydroxyl radicals (HO^\bullet) and not the subsequent recombination products [3]. With the correction factors mentioned previously (experimental setup – radical yield), an approximation of the actual radical production can be made. At 10 bar driving pressure for MD-A, the cumulative rate of 1110 photons/s corresponds to $1.25 \cdot 10^7$ HO^\bullet /s. For MD-B, this rate is much lower at $1.55 \cdot 10^6$ HO^\bullet /s, yet in the same range as prior observations with the global acquisition technique ($2.15 \cdot 10^6$ HO^\bullet /s) [33] at 10 bar driving pressure for the same channel. For both channels, the radical yield for both channels increases at a steady linear rate with regards to driving pressure, as can be seen in Fig. 6a. For the device MD-A at 10 bar, the gradually emerging second symmetric vapour pocket is accompanied by an almost twofold increase of the radical yield. However, the liquid line on the experiment does not allow us to perform experiments for pressure above 10 bar, which would shed light on the evolution of the double stream regime. The two different rates for MD-A and MD-B are probably caused by the vastly different geometrical conditions (Fig. 6b), while the insert in the figure shows the evolution of the radical

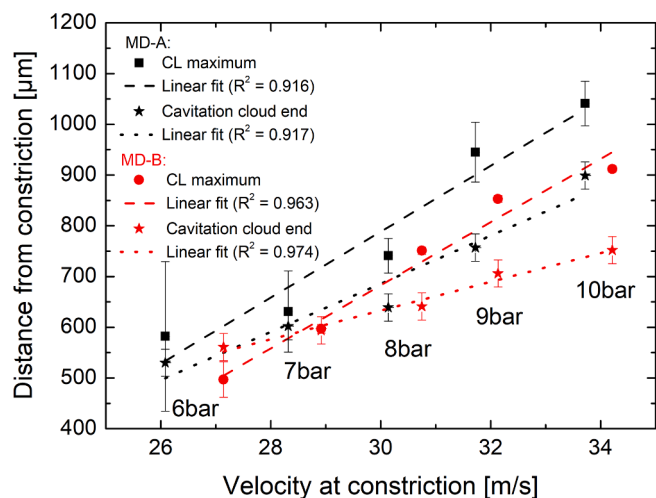


Fig. 5. MD-A and MD-B channel: the distance of the maximum CL activity (circle), the cavitation cloud end (star) from the diaphragm opening at different jet velocities emerging from the constriction (driving pressures indicated). The dashed and dotted lines show the linear fit of the individual data series. Error in x axis smaller than symbol size.

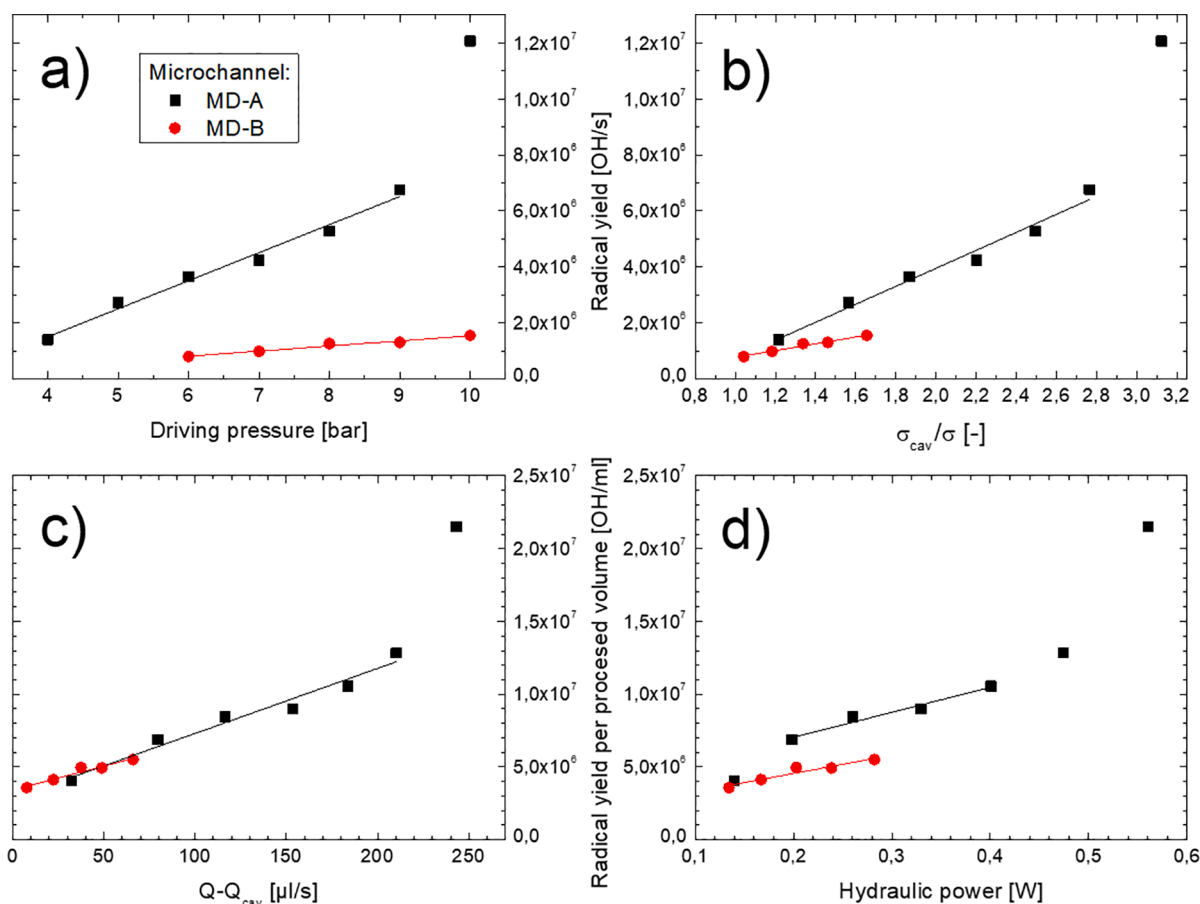


Fig. 6. Radical production figures for the MD-A (black) and MD-B (red). a) Radical yield at different driving pressures b) radical yield as a function of $\sigma_{\text{cav}}/\sigma$ parameter, c) radical yield per processed volume as a function of the $Q-Q_{\text{cav}}$ parameter (volume flow above cavitation inception flow), d) radical yield per processed volume at different hydraulic power. Error bars in x and y are smaller than symbol size.

production with the $\sigma_{\text{cav}}/\sigma$ parameter. The latter shows that at cavitation inception, both channels had roughly the same production rate, which then follow their respective rate as the driving pressure and the vapour cloud increase. This indicates some inherent similarities between the channels, which are further emphasized on Fig. 6c, as the geometrical differences between the channels seem to fade away when observing the radical yield per processed volume at different $Q-Q_{\text{cav}}$ values. Similarly, the radical production per treated liquid volume, increases linearly when plotted as a function of hydraulic power ($\Delta P \cdot Q$), in Fig. 6d. In the single pocket regime, the respective slopes display similar values (for MD-A $k_{\text{MD-A}} = 1.71 \cdot 10^7$ and the MD-B $k_{\text{MD-B}} = 1.25 \cdot 10^7$ OH/ml/W). This is most-likely due to the gradual expansion of the single pocket flow regime. This holds throughout the MD-B pressure range and from 5 to 8 bar for the MD-A, as it starts transitioning to the twin pocket regime at higher pressures. The characteristics of the device MD-B and the limitations of the experimental setup did not permit us to explore the two-pocket supercavitating flow, which could confirm whether it is a general trend of the microdiaphragm design. The maximum radical production per litre of sample treated was $2.15 \cdot 10^{10}$ HO'/l, at approximately 0.56 W hydraulic power (MD-A at 10 bar), corresponding to $3.84 \cdot 10^{10}$ HO'/(l*W). This is in accordance with the previous findings [33]. Arrojo et al. [25] used a macroscopic hydrodynamic reactor with salicylic acid dosimetry and a 2 kW pump and obtained values roughly one order of magnitude higher ($2.6 \cdot 10^{11}$ HO'/(l*W)), while not considering the possible cavitation events in the suction part of the driving pump. Other studies on the subject found in ultrasonic cavitation the rate of $6.6 \cdot 10^5$ HO'/cycle at 52 kHz making it around $3.4 \cdot 10^{10}$ HO'/s [66], however different bubble dynamics and lack of power input and processed volume data make direct comparison difficult.

When considering HC, our results suggest that the size of the vapour clouds, should be the key parameter related to CL activity. Moreover, this technique goes beyond the localisation of radical production. A single photon detected by the photon counting technique, indicates a hydroxyl radical oxidising a molecule of luminol, thus providing the number of reacting radicals. From a more general point of view, this can give a realistic estimation of the expected oxidation reactions from HC reactors, as the CL reaction with the highly reactive radicals can also be considered a model reaction between the produced radicals and organic matter in water. Therefore, by monitoring the CL activity in the reactor, a quick and simple technique for optimisation and fast prototyping of HC reactors is possible. This can give a reasonable estimation of the expected oxidation reactions for cavitation-based wastewater treatment solutions and other advance oxidising processes.

4. Conclusions

A novel technique for determining the chemiluminescent active region in hydrodynamic cavitation reactors, fed with a luminol solution, has been developed. Upgrading a previous global technique, which provided only the total emitted photon numbers, the new approach allows us to determine the collapse area in the flow. The position where the maximum chemiluminescent activity is recorded, indicates where hydroxyl radicals react with luminol. Correlations with the void fraction data have proven that light emission follows the cavitation clouds collapse. Furthermore, radical quantification was possible, as the technique allows for single photon detection. The current CL mapping technique can be used for rapid prototyping of micro and could be scaled up to macro hydrodynamic cavitation reactors. This would enable us to

optimise channel design or other flow parameters for radical production. Microfluidic systems were found to have bubble lifetimes in the range of a single half period (rarefaction) in a low frequency ultrasound process. The technique demonstrates that even weak emission from systems like hydrodynamic cavitation in microchannels can be characterised and allow us to obtain its radical yield. This makes it an important and easily implementable tool for future work on waste-water treatment devices and other advanced oxidation processes.

CRedit authorship contribution statement

Darjan Podbevšek: Conceptualization, Data curation, Formal analysis, Investigation, Methodology, Visualization, Writing - original draft. **Damien Colombet:** Investigation, Visualization, Resources, Writing - review & editing. **Frederic Ayela:** Conceptualization, Writing - review & editing. **Gilles Ledoux:** Conceptualization, Formal analysis, Methodology, Supervision, Writing - review & editing.

Declaration of Competing Interest

The authors declare that they have no known competing financial interests or personal relationships that could have appeared to influence the work reported in this paper.

Acknowledgments

The authors would like to thank A. Mishra for the acquisition and treatment of shadowgraphy images, as well as Y. Guillin, J.F. Sivignon and V. Menu for help with the construction of the experimental setup.

References

- [1] K.S. Suslick, The chemical effects of ultrasound, *Sci. Am.* 260 (1989) 80–86, <https://doi.org/10.1038/scientificamerican0289-80>.
- [2] M. Ashokkumar, The characterization of acoustic cavitation bubbles – an overview, *Ultrason. Sonochem.* 18 (2011) 864–872, <https://doi.org/10.1016/j.ultsonch.2010.11.016>.
- [3] H.N. McMurray, B.P. Wilson, Mechanistic and spatial study of ultrasonically induced luminol chemiluminescence, *J. Phys. Chem. A* 103 (1999) 3955–3962, <https://doi.org/10.1021/jp984503r>.
- [4] M. Gagol, A. Przyjazny, G. Boczkaj, Wastewater treatment by means of advanced oxidation processes based on cavitation – a review, *Chem. Eng. J.* 338 (2018), <https://doi.org/10.1016/j.cej.2018.01.049>.
- [5] R.J. Wood, J. Lee, M.J. Bussemaker, A parametric review of sonochemistry: control and augmentation of sonochemical activity in aqueous solutions, *Ultrason. Sonochem.* 38 (2017) 351–370, <https://doi.org/10.1016/j.ultsonch.2017.03.030>.
- [6] M. Zupanc, Z. Pandur, T. Stepišnik Perdih, D. Stopar, M. Petkovšek, M. Dular, Effects of cavitation on different microorganisms: The current understanding of the mechanisms taking place behind the phenomenon. A review and proposals for further research, *Ultrason. Sonochem.* 57 (2019) 147–165, <https://doi.org/10.1016/j.ultsonch.2019.05.009>.
- [7] B. Gielen, S. Marchal, J. Jordens, L.C.J. Thomassen, L. Braeken, T. Van Gerven, Influence of dissolved gases on sonochemistry and sonoluminescence in a flow reactor, *Ultrason. Sonochem.* 31 (2016) 463–472, <https://doi.org/10.1016/j.ultsonch.2016.02.001>.
- [8] J. Rooze, E.V. Rebrov, J.C. Schouten, J.T.F. Keurentjes, Dissolved gas and ultrasonic cavitation – a review, *Ultrason. Sonochem.* 20 (2013) 1–11, <https://doi.org/10.1016/j.ultsonch.2012.04.013>.
- [9] K.A. Mørch, Reflections on cavitation nuclei in water, *Phys. Fluids* 19 (2007), 072104, <https://doi.org/10.1063/1.2747210>.
- [10] S. Arrojo, Y. Benito, A theoretical study of hydrodynamic cavitation, *Ultrason. Sonochem.* 15 (2008) 203–211, <https://doi.org/10.1016/j.ultsonch.2007.03.007>.
- [11] M. Sivakumar, A.B. Pandit, Wastewater treatment: a novel energy efficient hydrodynamic cavitation technique, *Ultrason. Sonochem.* 9 (2002) 123–131.
- [12] K.S. Suslick, M.M. Mdeleeni, J.T. Ries, Chemistry induced by hydrodynamic cavitation, *J. Am. Chem. Soc.* 119 (1997) 9303–9304, <https://doi.org/10.1021/ja972171i>.
- [13] P.R. Gogate, I.Z. Shirgaonkar, M. Sivakumar, P. Senthilkumar, N.P. Vichare, A. B. Pandit, Cavitation reactors: efficiency assessment using a model reaction, *AIChE J.* 47 (2001) 2526–2538, <https://doi.org/10.1002/aic.690471115>.
- [14] P.R. Gogate, A.B. Pandit, A review and assessment of hydrodynamic cavitation as a technology for the future, *Ultrason. Sonochem.* 12 (2005) 21–27, <https://doi.org/10.1016/j.ultsonch.2004.03.007>.
- [15] S.K. Pawar, A.V. Mahulkar, A.B. Pandit, K. Roy, V.S. Moholkar, Sonochemical effect induced by hydrodynamic cavitation: comparison of venturi/orifice flow geometries, *AIChE J.* 63 (2017) 4705–4716, <https://doi.org/10.1002/aic.15812>.
- [16] A.A. Batoeva, D.G. Aseev, M.R. Szyzkyh, I.N. Vol'nov, A study of hydrodynamic cavitation generated by low pressure jet devices, *Russ. J. Appl. Chem.* 84 (2011) 1366, <https://doi.org/10.1134/S107042721108012X>.
- [17] D.G. Aseev, A.A. Batoeva, Effect of hydrodynamic cavitation on the rate of OH-radical formation in the presence of hydrogen peroxide, *Russ. J. Phys. Chem. A* 88 (2014) 28–31, <https://doi.org/10.1134/S0036024413120030>.
- [18] S.Y. Tang, M. Sivakumar, A novel and facile liquid whistle hydrodynamic cavitation reactor to produce submicron multiple emulsions, *AIChE J.* 59 (2013) 155–167, <https://doi.org/10.1002/aic.13800>.
- [19] M. Schlender, K. Minke, H.P. Schuchmann, Sono-chemiluminescence (SCL) in a high-pressure double stage homogenization processes, *Chem. Eng. Sci.* 142 (2016) 1–11, <https://doi.org/10.1016/j.ces.2015.11.028>.
- [20] Z. Zhang, G. Wang, Y. Nie, J. Ji, Hydrodynamic cavitation as an efficient method for the formation of sub-100nm O/W emulsions with high stability, *Chin. J. Chem. Eng.* 24 (2016) 1477–1480, <https://doi.org/10.1016/j.cjche.2016.04.011>.
- [21] K.A. Ramisetty, A.B. Pandit, P.R. Gogate, Novel approach of producing oil in water emulsion using hydrodynamic cavitation reactor, *Ind. Eng. Chem. Res.* 53 (2014) 16508–16515, <https://doi.org/10.1021/ie502753d>.
- [22] J. Carpenter, S. George, V.K. Saharan, Low pressure hydrodynamic cavitation device for producing highly stable oil in water emulsion: effect of geometry and cavitation number, *Chem. Eng. Process. Process Intensif.* 116 (2017) 97–104, <https://doi.org/10.1016/j.cep.2017.02.013>.
- [23] P. Braeutigam, Z.-L. Wu, A. Stark, B. Ondruschka, Degradation of BTEX in aqueous solution by hydrodynamic cavitation, *Chem. Eng. Technol.* 32 (2009) 745–753, <https://doi.org/10.1002/ceat.200800626>.
- [24] P. Braeutigam, M. Franke, Z.-L. Wu, B. Ondruschka, Role of different parameters in the optimization of hydrodynamic cavitation, *Chem. Eng. Technol.* 33 (2010) 932–940, <https://doi.org/10.1002/ceat.201000021>.
- [25] S. Arrojo, C. Nerín, Y. Benito, Application of salicylic acid dosimetry to evaluate hydrodynamic cavitation as an advanced oxidation process, *Ultrason. Sonochem.* 14 (2007) 343–349, <https://doi.org/10.1016/j.ultsonch.2006.06.007>.
- [26] X. Wang, J. Wang, P. Guo, W. Guo, C. Wang, Degradation of rhodamine B in aqueous solution by using swirling jet-induced cavitation combined with H₂O₂, *J. Hazard. Mater.* 169 (2009) 486–491, <https://doi.org/10.1016/j.jhazmat.2009.03.122>.
- [27] K.R. Morison, C.A. Hutchinson, Limitations of the Weisser reaction as a model reaction for measuring the efficiency of hydrodynamic cavitation, *Ultrason. Sonochem.* 16 (2009) 176–183, <https://doi.org/10.1016/j.ultsonch.2008.07.001>.
- [28] K.M. Kalumuck, G.L. Chahine, The use of cavitating jets to oxidize organic compounds in water, *J. Fluids Eng.* 122 (2000) 465–470, <https://doi.org/10.1115/1.1286993>.
- [29] K.J. Taylor, P.D. Jarman, Spectrum and lifetime of the acoustically and chemically induced emission of light from luminol, *J. Am. Chem. Soc.* 93 (1971) 257–258, <https://doi.org/10.1021/ja00730a047>.
- [30] V. Renaudin, N. Gondrexon, P. Boldo, C. Périer, A. Bernis, Y. Gonthier, Method for determining the chemically active zones in a high-frequency ultrasonic reactor, *Ultrason. Sonochem.* 1 (1994) S81–S85, [https://doi.org/10.1016/1350-4177\(94\)90002-7](https://doi.org/10.1016/1350-4177(94)90002-7).
- [31] S.-W. Tandiono, D.S.W. Ohl, E. Ow, V.V. Klaseboer, R. Wong, C.-D. Dumke, Ohl, Sonochemistry and sonoluminescence in microfluidics, *Proc. Natl. Acad. Sci.* 108 (2011) 5996–5998, <https://doi.org/10.1073/pnas.1019623108>.
- [32] S.-I. Hatanaka, H. Mitome, K. Yasui, S. Hayashi, Single-bubble sonochemiluminescence in aqueous luminol solutions, *J. Am. Chem. Soc.* 124 (2002) 10250–10251.
- [33] D. Podbevšek, D. Colombet, G. Ledoux, F. Ayela, Observation of chemiluminescence induced by hydrodynamic cavitation in microchannels, *Ultrason. Sonochem.* 43 (2018) 175–183, <https://doi.org/10.1016/j.ultsonch.2018.01.004>.
- [34] T. Stieger, H. Agha, M. Schoen, M.G. Mazza, A. Sengupta, Hydrodynamic cavitation in Stokes flow of anisotropic fluids, *Nat. Commun.* 8 (2017) 15550, <https://doi.org/10.1038/ncomms15550>.
- [35] F. Ayela, M. Medrano-Muñoz, D. Amans, C. Dujardin, T. Brichtart, M. Martini, O. Tillement, G. Ledoux, Experimental evidence of temperature gradients in cavitating microflows seeded with thermosensitive nanoprobe, *Phys. Rev. E Stat. Nonlin. Soft Matter Phys.* 88 (2013), 043016, <https://doi.org/10.1103/PhysRevE.88.043016>.
- [36] M. Medrano, P.J. Zermatten, C. Pellone, J.P. Franc, F. Ayela, Hydrodynamic cavitation in microsystems. I. Experiments with deionized water and nanofluids, *Phys. Fluids* 23 (2011), 127103, <https://doi.org/10.1063/1.3671682>.
- [37] C. Mishra, Y. Peles, Cavitation in flow through a micro-orifice inside a silicon microchannel, *Phys. Fluids* 17 (2004), 013601, <https://doi.org/10.1063/1.1827602>.
- [38] M. Medrano, C. Pellone, P.J. Zermatten, F. Ayela, Hydrodynamic cavitation in microsystems. II. Simulations and optical observations, *Phys. Fluids* 24 (2012), 047101, <https://doi.org/10.1063/1.3699067>.
- [39] Y. Peles, B. Schneider, Hydrodynamic cavitation and boiling in refrigerant (R-123), *Flow Inside Microchannels* (2006) 1323–1332, <https://doi.org/10.1115/ICNMM2006-96030>.
- [40] G.S. Cole, R.P. Scaringe, R.P. Roth, Y. Peles, System Evaluation of Cavitation Enhanced Heat Transfer in Microchannels, *SAE International*, Warrendale, PA, 2006. <https://doi.org/10.4271/2006-01-3062>.
- [41] C. Mishra, Y. Peles, Flow visualization of cavitating flows through a rectangular slot micro-orifice ingrained in a microchannel, *Phys. Fluids* 17 (2005), 113602, <https://doi.org/10.1063/1.2132289>.

- [42] C. Mishra, Y. Peles, An experimental investigation of hydrodynamic cavitation in micro-Venturis, *Phys. Fluids*. 18 (2006), 103603, <https://doi.org/10.1063/1.2360996>.
- [43] C. Mishra, Y. Peles, Development of cavitation in refrigerant (R-123) flow inside rudimentary microfluidic systems, *J. Microelectromechanical Syst.* 15 (2006) 1319–1329, <https://doi.org/10.1109/JMEMS.2006.872230>.
- [44] C. Mishra, Y. Peles, Size scale effects on cavitating flows through microorifices entrenched in rectangular microchannels, *J. Microelectromechanical Syst.* 14 (2005) 987–999, <https://doi.org/10.1109/JMEMS.2005.851800>.
- [45] C. Mishra, Y. Peles, Hydrodynamic Cavitation in Flow Through Micro-Constriction Elements Entrenched in Rectangular Microchannels, (2005) 761–770. <https://doi.org/10.1115/FEDSM2005-77406>.
- [46] A. Nayebzadeh, Y. Wang, H. Tabkhi, J.-H. Shin, Y. Peles, Cavitation behind a circular micro pillar, *Int. J. Multiph. Flow*. 98 (2018) 67–78, <https://doi.org/10.1016/j.ijmultiphaseflow.2017.08.012>.
- [47] B. Schneider, A. Koşar, Y. Peles, Hydrodynamic cavitation and boiling in refrigerant (R-123) flow inside microchannels, *Int. J. Heat Mass Transf.* 50 (2007) 2838–2854, <https://doi.org/10.1016/j.ijheatmasstransfer.2007.01.002>.
- [48] F. Ayela, W. Cherief, D. Colombet, G. Ledoux, M. Martini, S. Mossaz, D. Podbevšek, X. Qiu, O. Tillement, Hydrodynamic Cavitation through “Labs on a Chip”: From Fundamentals to Applications, *Oil Gas Sci. Technol. – Rev. D’IFP Energ. Nouv.* 72 (2017) 19, <https://doi.org/10.2516/ogst/2017010>.
- [49] R. Singh, Y. Peles, The effects of fluid properties on cavitation in a micro domain, *J. Micromechanics Microengineering*. 19 (2009), 025009, <https://doi.org/10.1088/0960-1317/19/2/025009>.
- [50] S. Mossaz, D. Colombet, F. Ayela, Hydrodynamic cavitation of binary liquid mixtures in laminar and turbulent flow regimes, *Exp. Therm. Fluid Sci.* 80 (2017) 337–347, <https://doi.org/10.1016/j.expthermflusci.2016.08.001>.
- [51] M. Ghorbani, A.K. Sadaghiani, L.G. Villanueva, A. Koşar, Hydrodynamic cavitation in microfluidic devices with roughened surfaces, *J. Micromechanics Microengineering*. 28 (2018), 075016, <https://doi.org/10.1088/1361-6439/aab9d0>.
- [52] M. Ghorbani, C. Sozer, G. Alcan, M. Unel, S. Ekici, H. Uvet, A. Koşar, Biomedical device prototype based on small scale hydrodynamic cavitation, *AIP Adv.* 8 (2018), 035108, <https://doi.org/10.1063/1.5005048>.
- [53] M. Ghorbani, A.K. Sadaghiani, M. Yidiz, A. Koşar, Experimental and numerical investigations on spray structure under the effect of cavitation phenomenon in a microchannel, *J. Mech. Sci. Technol.* 31 (2017) 235–247, <https://doi.org/10.1007/s12206-016-1226-y>.
- [54] M. Ghorbani, A. Mohammadi, A.R. Motezakker, L.G. Villanueva, Y. Leblebici, A. Koşar, Energy Harvesting in Microscale with Cavitating Flows, *ACS Omega* 2 (2017) 6870–6877, <https://doi.org/10.1021/acsomega.7b01204>.
- [55] J. Rooze, M. André, G.-J.S. van der Gulik, D. Fernández-Rivas, J.G.E. Gardeniers, E. V. Rebroy, J.C. Schouten, J.T.F. Keurentjes, Hydrodynamic cavitation in micro channels with channel sizes of 100 and 750 micrometers, *Microfluid. Nanofluidics*. 12 (2012) 499–508, <https://doi.org/10.1007/s10404-011-0891-5>.
- [56] T. Gothsch, C. Schilcher, C. Richter, S. Beinert, A. Dietzel, S. Büttgenbach, A. Kwade, High-pressure microfluidic systems (HPMS): flow and cavitation measurements in supported silicon microsystems, *Microfluid. Nanofluidics*. 18 (2015) 121–130, <https://doi.org/10.1007/s10404-014-1419-6>.
- [57] X. Qiu, W. Cherief, D. Colombet, F. Ayela, A simple process to achieve microchannels geometries able to produce hydrodynamic cavitation, *J. Micromechanics Microengineering*. 27 (2017), 047001, <https://doi.org/10.1088/1361-6439/aa5fa5>.
- [58] X. Qiu, V. Bouchiat, D. Colombet, F. Ayela, Liquid-phase exfoliation of graphite into graphene nanosheets in a hydrocavitating ‘lab-on-a-chip’, *RSC Adv.* 9 (2019) 3232–3238, <https://doi.org/10.1039/C8RA05976D>.
- [59] A.S. Aghdam, M. Ghorbani, G. Deprem, F.Ç. Cebeci, A. Koşar, A New Method for Intense Cavitation Bubble Generation on Layer-by-Layer Assembled SLIPS, *Sci. Rep.* 9 (2019) 1–13, <https://doi.org/10.1038/s41598-019-48175-4>.
- [60] M. Ghorbani, H. Chen, L.G. Villanueva, D. Grishenkov, A. Koşar, Intensifying cavitating flows in microfluidic devices with poly(vinyl alcohol) (PVA) microbubbles, *Phys. Fluids*. 30 (2018), 102001, <https://doi.org/10.1063/1.5051606>.
- [61] M.T. Gevari, M. Ghorbani, A.J. Svagan, D. Grishenkov, A. Kosar, Energy harvesting with micro scale hydrodynamic cavitation-thermoelectric generation coupling, *AIP Adv.* 9 (2019), 105012, <https://doi.org/10.1063/1.5115336>.
- [62] J. Lee, H.H. Seliger, Quantum Yields of the Luminol Chemiluminescence Reaction in Aqueous and Aprotic Solvents*, *Photochem. Photobiol.* 15 (1972) 227–237, <https://doi.org/10.1111/j.1751-1097.1972.tb06241.x>.
- [63] A.G. Siraki, L.-O. Klotz, J.P. Kehrler, 1.14 - Free Radicals and Reactive Oxygen Species*, in: C.A. McQueen (Ed.), *Compr. Toxicol. Third Ed.*, Elsevier, Oxford, 2018, pp. 262–294. <https://doi.org/10.1016/B978-0-12-801238-3.01895-X>.
- [64] J.M. Burns, W.J. Cooper, J.L. Ferry, D.W. King, B.P. DiMento, K. McNeill, C. J. Miller, W.L. Miller, B.M. Peake, S.A. Rusak, A.L. Rose, T.D. Waite, Methods for reactive oxygen species (ROS) detection in aqueous environments, *Aquat. Sci.* 74 (2012) 683–734, <https://doi.org/10.1007/s00027-012-0251-x>.
- [65] P. Attri, Y.H. Kim, D.H. Park, J.H. Park, Y.J. Hong, H.S. Uhm, K.-N. Kim, A. Fridman, E.H. Choi, Generation mechanism of hydroxyl radical species and its lifetime prediction during the plasma-initiated ultraviolet (UV) photolysis, *Sci. Rep.* 5 (2015) 1–8, <https://doi.org/10.1038/srep09332>.
- [66] Y.T. Didenko, K.S. Suslick, The energy efficiency of formation of photons, radicals and ions during single-bubble cavitation, *Nature* 418 (2002) 394–397, <https://doi.org/10.1038/nature00895>.